

Radar interferogram filtering for geophysical applications

Richard M. Goldstein and Charles L. Werner

Jet Propulsion Laboratory, California Institute of Technology, Pasadena, California

Abstract. The use of SAR interferometry is often impeded by decorrelation from thermal noise, temporal change, and baseline geometry. Power spectra of interferograms are typically the sum of a narrow-band component combined with broad-band noise. We describe a new adaptive filtering algorithm that dramatically lowers phase noise, improving both measurement accuracy and phase unwrapping, while demonstrating graceful degradation in regions of pure noise. The performance of the filter is demonstrated with SAR data from the ERS satellites over the Jakobshavns glacier of Greenland.

1. Introduction

Synthetic aperture radar (SAR) interferometry is a powerful technique for measurement of the earth surface. Applications include generation of high resolution topographic maps [Li and Goldstein 1990], measurement of flow in glaciers and ice sheets [Goldstein et al. 1993; Joughin et al. 1996], and surface displacement associated with crustal deformation [Massonnet et al. 1993; Peltzer and Rosen 1995].

Acquisition of interferometric SAR data requires two or more passes over a site with an imaging geometry as shown in Figure 1. Interferometric measurements may be separated in space and or time depending on the specific application or system. Studies of processes that evolve in time, such as glacial flow or tectonic plate motion require data acquisitions at differing times to detect the motion that occurs between observations. Conversely, the optimum strategy for topographic mapping requires simultaneous acquisition of the images forming the interferometric pair, thereby avoiding temporal decorrelation in the scene and the phase distortions arising from ionospheric and tropospheric turbulence [Goldstein 1995].

Differential interferometry measures changes in the line-of-sight distance that occurs during the time interval between SAR data acquisitions. The error sensitivity of the displacement σ_r to the differential phase measurement error σ_ϕ is

$$\sigma_r = \frac{\lambda}{4\pi} \sigma_\phi, \quad (1)$$

where λ is the radar wavelength.

Copyright 1998 by the American Geophysical Union.

Paper number 1998900033.
0094-8276/98/GL-1998900033\$05.00

Topographic mapping uses the interferometric phase to measure the difference in the slant range from points separated by the baseline B . The standard deviation of the height σ_h is linearly proportional to the interferometric phase standard deviation σ_ϕ :

$$\sigma_h = \frac{\lambda}{4\pi} \left| \frac{\rho \sin \theta}{B \cos(\theta - \alpha)} \right| \sigma_\phi, \quad (2)$$

and a function of the slant range ρ , look angle θ , baseline length B , and baseline tilt angle α .

Sources of phase noise in the interferograms include baseline geometry, thermal noise, and temporal changes in the radar backscatter relating to scene rotation, disturbances of the ground cover or forest canopy, and erosion [Zebker and Villasenor 1992]. Scene related temporal decorrelation is a very serious limitation to the general application of differential interferometry on a global basis.

2. Interferogram Filtering Algorithm

The interferogram power spectra of most regions is characterized by a "white" component, generated by thermal noise and loss of correlation, and a narrow band component, related to the fringes. The local fringe rate

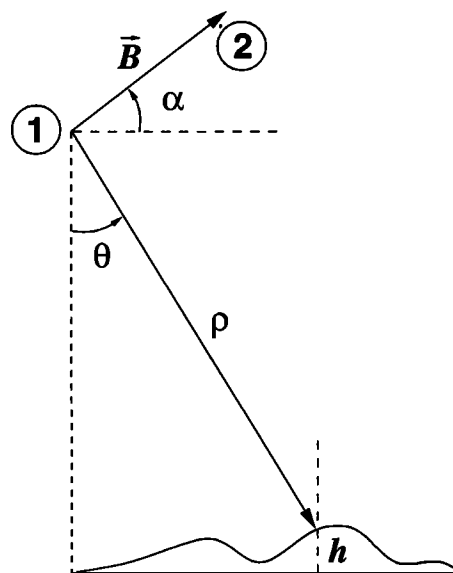


Figure 1. Interferometric imaging geometry. The vector between radar tracks is the baseline B rotated by the tilt angle α relative to a horizontal reference. The look vector with length ρ points from the radar to the surface with look angle θ .

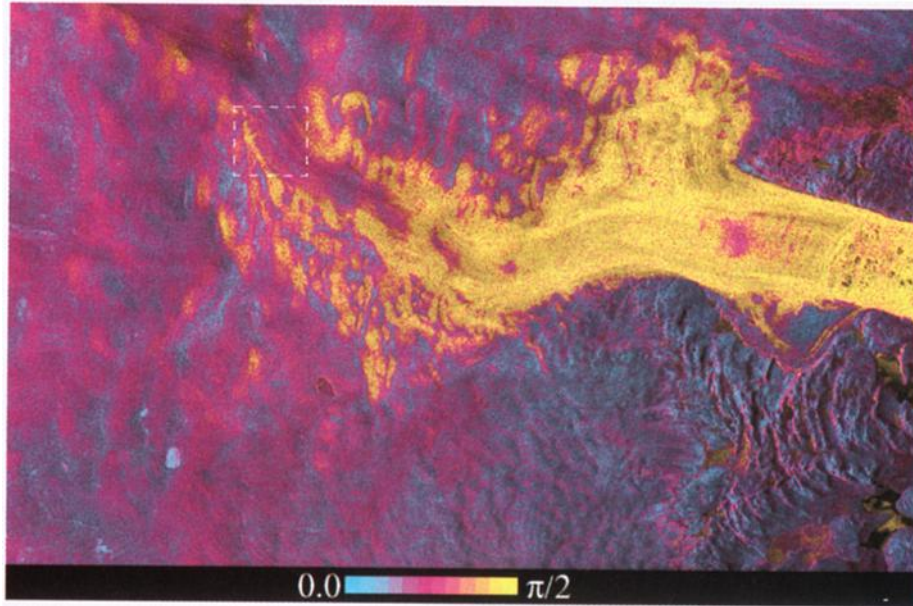


Figure 2. Phase standard deviation of ERS-1/ERS-2 Tandem interferogram of Jakobshavns Glacier in North East Greenland (69°10' N, 49°5' W). The scene is approximately 68.6 x 43.5 km and is color coded for the local phase standard deviation σ_ϕ over the range $[0, \pi/2]$. Regions near the exit of the glacier are completely decorrelated leading to a high σ_ϕ caused by glacier motion over the 1-day interval. Intensity of the image is proportional to the radar brightness of the scene. For these data, 5 samples were averaged in azimuth such that the output sample spacing is approximately 20×20 meters. The result of the new algorithm applied to the marked rectangular region of the interferogram are shown in Figure 3.

is determined by the look angle, along-track changes in the baseline, and any motion of the scene along the line of sight. The contribution from topography and the baseline geometry usually dominates and is given by:

$$\frac{d\phi}{d\rho} = \frac{4\pi B \cos(\theta - \alpha)}{\lambda \rho \tan \theta} . \quad (3)$$

In other cases, such as along glacier margins, the interferometric phase is mainly due to motion. Phase unwrapping is necessary to resolve the unknown multiple-of-wavelength ambiguity in the interferometric phase and thereby determine the motion. Regions of high deformation are characterized by increased phase noise and high local fringe rates. These factors preclude accurate unwrapping unless an effective filtering algorithm is employed that reduces the phase noise.

The non-stationarity of the fringe spectrum requires an adaptive filtering algorithm sensitive to the local phase noise and fringe rate. The interferogram $I(x,y)$ is segmented into overlapping rectangular patches and the power spectrum $Z(u,v)$ for each patch is computed by smoothing the intensity of the two-dimensional FFT. The response of the adaptive filter $H(u,v)$ is then computed from the power spectrum:

$$H(u,v) = |Z(u,v)|^\alpha . \quad (4)$$

For the case where the filter parameter $\alpha = 0$, no filtering occurs, while for $\alpha = 1$ the filtering is strong. Useful values of α lie in the range 0.2 to 1. Interferograms with

very low correlation benefit from larger patch sizes and higher values of α . Patches are overlapped to attenuate discontinuities at the boundaries. Overlap in our implementation is 75% for both the along-track and cross-track directions with triangular weighting of the filtered data. The effect of this window is to obtain the sum of weighted contributions from each of the patches that cover a particular interferogram sample.

The spatial resolution of the filter adapts to the local phase variation such that regions of smooth phase are strongly filtered, while regions with high phase variance are weakly filtered. A simple example demonstrates the filter resolution and noise properties. Consider a two-dimensional Gaussian shaped power spectrum of the form

$$Z(u,v) = \exp \left\{ -\frac{\frac{u^2}{\sigma_u^2} - \frac{2uv}{\sigma_u \sigma_v} + \frac{v^2}{\sigma_v^2}}{2(1 - \rho^2)} \right\} . \quad (5)$$

The input has effective bandwidths σ_u and σ_v for the u and v frequency coordinates respectively. After filtering the bandwidth is reduced to $\sigma_u/\sqrt{1+\alpha}$ and $\sigma_v/\sqrt{1+\alpha}$. For the case of $\alpha = 1$, the bandwidth is reduced by half in each dimension and the effective signal to noise ratio is squared. The consequence of filtering the interferometric phase can be observed by subtracting the filtered interferometric phase from the unfiltered interferogram. Any residual systematic phase trend in the difference indicates that filtering has led to some loss of resolution in the filtered phase.

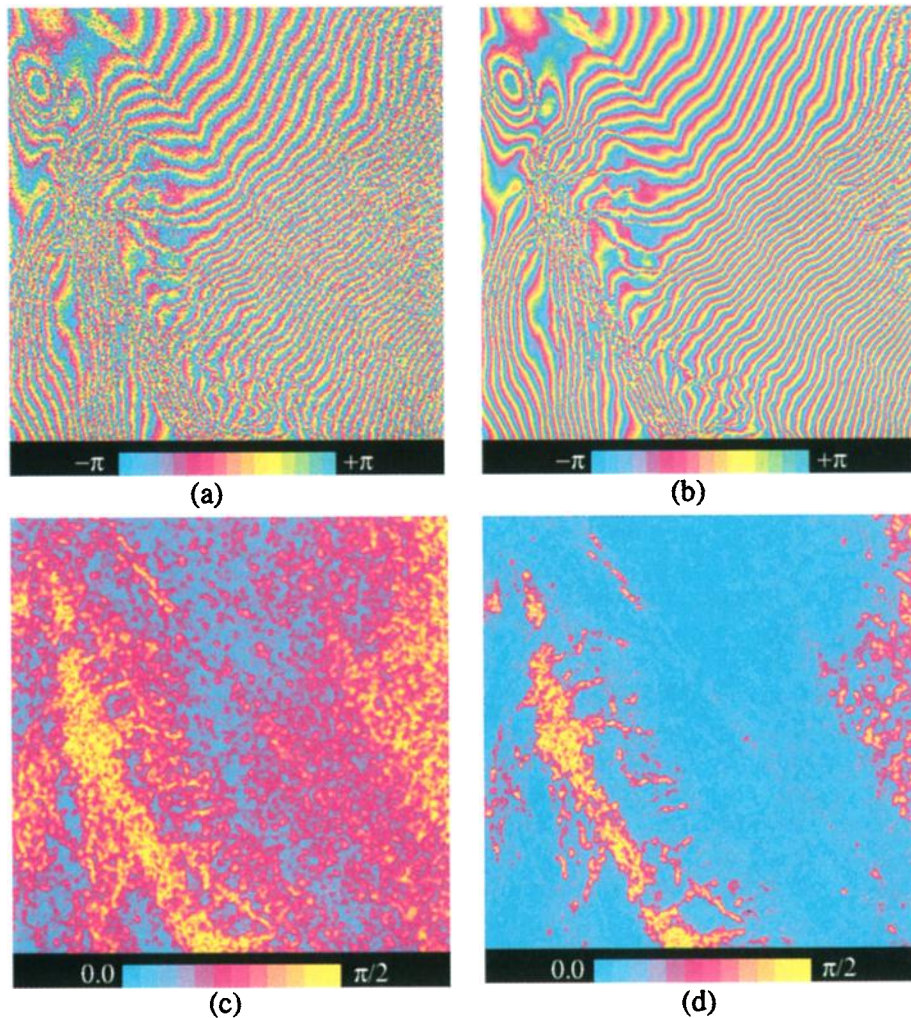


Figure 3. Comparison of unfiltered and filtered interferograms ($\alpha = 1$) of Jakobshavns glacier. The standard deviation of the phase was evaluated using a 5×5 estimation window after subtraction of the local phase ramp. Resolution element size is approximately 20×20 meters. The interferogram phase is wrapped between $-\pi$ and $+\pi$. (a) Unfiltered 5-look interferogram phase; (b) filtered interferometric phase; (c) σ_ϕ for the unfiltered interferogram; (d) σ_ϕ after filtering.

2.1. ERS Tandem Mission example from the Jakobshavns Glacier

Interferometric SAR data were collected over the Jakobshavns glacier in West Greenland by ERS-1 and ERS-2 on November 11 and November 12, 1995 and again 35 days later. ERS-1 and ERS-2 were in repeat orbits during the Tandem phase such that two co-registered interferograms could be produced from the 4 passes. The standard deviation of the interferometric phase of the glacier is shown in Figure 2. Over the 1-day acquisition interval rapid shear, rotation, and weathering in the lower reaches of the glacier cause significant decorrelation (high σ_ϕ). Upstream, noisy fringes are discernible. Regions with little motion or rock have high correlation (low σ_ϕ) consistent with little or no surface change.

An interferogram with non-zero baseline generally has fringes from both topography and deformation. Ad-

ditional information in the form of a digital elevation model or second interferogram is required to remove the topographic component. If a digital elevation model is available, a simulated interferogram can be generated and subtracted from the unwrapped interferogram to obtain motion along the line of sight [Rosen et al. 1996]. Alternately, if two interferograms with different baselines are available, then each can be unwrapped and a least squares fit over regions with no motion performed to determine the relative phase scaling between interferograms. The contribution of topography in one of the interferograms can then be removed using the fit parameters [Goldstein 1997; Gabriel et al. 1989].

The standard deviation of the phase σ_ϕ is a meaningful measure of interferometric noise and can be estimated directly from the interferogram, both before and after filtering. Estimation of σ_ϕ is carried out after removal of a locally linear phase ramp $\tilde{\phi}(i, j)$ over a rectangular window centered on the point,

$$\sigma_\phi = \left(\frac{\sum_N (\phi(i, j) - \bar{\phi}(i, j))^2}{N-1} \right)^{\frac{1}{2}}, \quad (6)$$

where N is the number of samples in the window. The phase slopes used to calculate $\bar{\phi}(i, j)$ are obtained by averaging the first differences of the complex interferogram samples in range and azimuth respectively [Madsen 1989]. In this example, the along-track and cross-track window widths for estimating σ_ϕ were 5 ($N = 25$).

Results from applying the filter ($\alpha = 1$) for a segment of the glacier interferogram are shown in Figure 3 along with maps of σ_ϕ before and after filtering. This particular interferogram segment was chosen because it contains areas of rapidly changing fringes, normal fringes, and featureless noise that illustrate the filter response in each of these regimes. The value of σ_ϕ was reduced from 0.68 to 0.19 radians in the first 32 lines of the image segment. Over the entire segment σ_ϕ improved from 0.78 to 0.33 radians. Since the filter is derived from the power spectrum, the filter has a broadband characteristic in noisy regions, but in areas where there are discernible fringes, narrow bandpass filtering occurs.

Phase unwrapping was performed using a residue based algorithm [Goldstein et al. 1988]. In this approach residues are points of two-dimensional phase inconsistency found by summation of the phase differences around closed paths. Branch cuts between residues in the interferogram plane are used to restrict the phase integration path such that consistent values of the unwrapped phase are obtained. Pure spatially uncorrelated noise can be shown to be 1/3 residues [Li and Goldstein 1990]. As the band-area of the filter decreases, the fraction of residues decreases linearly resulting in larger mean distance between residues. The number of residues in the unfiltered interferogram segment is 8551. After filtering the number of residues is reduced to 1700 and the vast majority of these are located in regions with no discernible fringes. The high density of residues in the remaining uncorrelated areas results in intersecting branch cuts that exclude phase unwrapping when using branch cut methods. A constant bandwidth non-adaptive filter will reduce the residue density even in areas with zero correlation leading to an increased probability of unwrapping errors. Using the new adaptive filter algorithm, 92% of the test interferogram segment could be unwrapped, compared with 64% of the unfiltered segment.

3. Conclusions

The adaptive interferogram filtering algorithm significantly improves fringe visibility and reduces phase noise introduced by scene dependent or system related decorrelation. The variable bandpass characteristic of the filter, derived directly from the power spectrum of the fringes preferentially smoothes the phase in regions with high correlation, but remains broad-band in regions of low correlation. The filter is very effective for improving the performance of branch-cut phase unwrapping methods because it reduces the number of residues in regions with discernible fringes, while preserving a high density

of residues in noisy regions. These characteristics exclude regions with a high probability of unwrapping error while significantly increasing the unwrapped image fraction permitting retrieval of topography or surface deformation over larger areas.

Acknowledgments. The authors are grateful to R. Bamler of DLR for suggestions relating to power spectrum estimation and to P. Rosen of JPL for his helpful comments. This work was performed at the Jet Propulsion Laboratory, California Institute of Technology under contract with the National Aeronautics and Space Administration. The European Space Agency provided raw SAR data of the Jakobshavn glacier to ESA PI R. M. Goldstein.

References

- Gabriel, A. K., R. M. Goldstein, and H. A. Zebker, Mapping small elevation changes over large areas: differential radar interferometry, *J. Geophys. Res.*, **94**, 9183-9191, 1989.
- Goldstein, R. M., H. A. Zebker, and C. L. Werner, Satellite radar interferometry: Two-dimensional phase unwrapping, *Radio Science*, **23**, 713-720, 1988.
- Goldstein, R. M., H. Engelhardt, B. Kamb, and R. M. Frollich, Satellite radar interferometry for monitoring ice sheet motion: application to an Antarctic ice stream, *Science*, **262**, 1525-1530, 1993.
- Goldstein, R. M., Atmospheric limitations to repeat-track radar interferometry, *Geophys. Res. Lett.*, **22**, 2517-2520, 1995.
- Goldstein, R. M., and C. L. Werner, Radar Ice Motion Interferometry, *Proc. 3rd ERS ESA Symposium*, *ESA SP-414*, 969-972, 1997.
- Joughin, I., R. Kwok, and M. Fahnestock, Estimation of ice sheet motion using satellite radar interferometry - method and error analysis with application to the Humboldt Glacier, Greenland, *J. Glaciology*, **42**, 564-575, 1996.
- Lee, J. S., K. Hoppel, S. Mango, and A. Miller, Intensity and phase statistics of multilook polarimetric and interferometric SAR imagery, *IEEE Trans. Geosci. and Remote Sensing*, **32**, 1017-1027, 1992.
- Li, F. K. and R. M. Goldstein, Studies of multi-baseline space-borne interferometric synthetic aperture radars, *IEEE Trans. Geosci. and Remote Sensing*, **28**, 88-97, 1990.
- Madsen, S. N. Estimating the doppler centroid of SAR data, *IEEE Trans. Aerosp. Electron. Syst.*, **25**, 134-140, 1989.
- Massonnet, D., M. Rossi, C. Carmona, F. Adragna, G. Peltzer, K. Fiegl, and T. Rabaute, The displacement field of the Landers earthquake mapped by radar interferometry, *Nature*, **364**, 138-142, 1993.
- Peltzer, G. and P. A. Rosen, Surface displacement of the 17 May 1993 Eureka Valley, California, earthquake observed by SAR interferometry, *Science*, **268**, 133-1336, 1995.
- Rosen, P. A., S. Hensley, H. A. Zebker, F. H. Webb, and E. J. Fielding, Surface deformation and coherence measurements of Kilauea Volcano, Hawaii, from SIR-C radar interferometry, *J. Geophys. Res.*, **101**, 23109-23125, 1996.
- Zebker, H. A., and J. Villasenor, Decorrelation in interferometric radar echoes, *IEEE Trans. Geosci. and Remote Sensing*, **30**, 950-959, 1992.
- Zebker, H. A., C. L. Werner, P. A. Rosen, and S. Hensley, Accuracy of topographic maps derived from ERS-1 interferometric radar, *IEEE Trans. Geosci. and Remote Sensing*, **32**, 823-836, 1994.

R. M. Goldstein and C. L. Werner, Jet Propulsion Laboratory, MS 300/227, 4800 Oak Grove Drive, Pasadena, CA 91109-8099. (e-mail: goldstein@kahuna.jpl.nasa.gov)

(Received Feb 26, 1998; revised July 13, 1998; accepted August 21, 1998.)